Radio Science

RESEARCH ARTICLE
10.1029/2018RS006662

Key Points:

- This study established space-time correlation schematics for analyzing and comparing correlation models in the context of spaced-receiver techniques
- A hybrid correlation model is proposed to estimate ionospheric drift velocity based on the front velocity model and the anisotropy model
- GNSS estimated drift velocities achieved favorable comparisons against ASI and PFISR measurements during a geomagnetic storm event

Correspondence to:
J. Wang,
jun.wang2@noaa.gov

Citation:
Wang, J., & Morton, Y. J. (2019). A hybrid correlation model for the spaced-receiver technique. *Radio Science*, *54*, 281–297. https://doi.org/10.1029/2018RS006662

Received 3 JUN 2018
Accepted 17 FEB 2019
Accepted article online 28 FEB 2019
Published online 27 MAR 2019

A Hybrid Correlation Model for the Spaced-Receiver Technique

Jun Wang[1,2] and Y. Jade Morton[3]

[1]Cooperative Institute for Research in Environmental Sciences, University of Colorado Boulder, Boulder, CO, USA, [2]Space Weather Prediction Center, National Oceanic and Atmospheric Administration, Boulder, CO, USA, [3]Smead Aerospace Engineering Sciences Department, University of Colorado Boulder, Boulder, CO, USA

Abstract A Global Navigation Satellite System (GNSS) spaced-receiver technique estimates ionospheric irregularity drift velocity by correlating the received GNSS signals across a closely spaced receiver array during ionospheric scintillations. This paper focuses on the correlation models accounting for the topology of the received diffraction pattern. Space-time correlation schematics are developed to analyze and compare several prevalent models, including the classic isotropy model, the front velocity model, and the anisotropy model. Based on the merits and drawbacks of each model, a hybrid correlation model is proposed, integrating the front velocity model and the anisotropy model. To validate the hybrid model, the corresponding drift velocity estimates are cross compared with the measurements from a colocated all-sky imager and incoherent scatter radar. A case study was conducted for a geomagnetic storm event on 20 December 2015. Favorable agreement was found in terms of direction and magnitude of the drift motion, orientation of the irregularity, temporal and spatial features of the irregularity, and the statistical behavior of the drift velocity estimates. In addition, the root-mean-square velocity magnitude and orientation against the incoherent scatter radar measurements demonstrate the superior performance of the hybrid model.

1. Introduction

A spaced-receiver technique estimates ionospheric irregularity drift velocity through analyzing transionospheric radio signals observed from a closely spaced receiver array (Briggs, 1968; Briggs et al., 1950; Mitra, 1949). Early studies focused on zonal drift estimation using signal intensity measurements in equatorial regions (Basu & Basu, 1981). Ultra high frequency and L band devices were used to receive radio signals transmitted from various satellite systems (Anderson & Mendillo, 1983; Basu et al., 1991; Vacchione et al., 1987). Because of their compact, low cost, and distributive nature, GPS receivers became increasingly popular in this research area (Basu et al., 1996; Kil et al., 2000, 2002; Kintner et al., 2004). With the modernization of Global Navigation Satellite System (GNSS), high-rate multi-GNSS carrier phase signals have been utilized in high-latitude regions (Su et al., 2017; Wang et al., 2018; Wang & Morton, 2015, 2017). The gist of the technique is to find the time delay between receiver measurements through cross correlation when similar diffraction pattern is observed on different receivers. Once the time delay (or time lag) is obtained, the diffraction pattern drift velocity can be inferred from the known receiver array baseline and a correlation model accounting for the shape of the correlation pattern caused by diffraction. Together with the satellite-receiver geometry and assumed effective irregularity height, the ionospheric irregularity drift velocity can be obtained (Kil et al., 2000).

In this study, prevalent correlation models for diffraction pattern drift velocity estimation are analyzed, including the classic isotropy model, the front velocity model, and the anisotropy model (Briggs et al., 1950; Fedor, 1967; Wang & Morton, 2017). Based on comparison of performances of these models with observations using a colocated all-sky imager and incoherent scatter radar, a hybrid correlation model is developed that combines results from the front velocity model and the anisotropy model. To validate this hybrid model, the corresponding irregularity drift velocity estimates are further cross compared against the all-sky imager and incoherent scatter radar measurements.

The classic correlation model was developed by Briggs et al. (1950). It implicitly assumes the received diffraction patterns induced by ionospheric irregularities to be isotropic. However, due to the high parallel conductivities of the ionosphere, the irregularities are expected to be elongated along Earth's magnetic field lines, causing highly anisotropic diffraction patterns (Mendillo & Baumgardner, 1982). Under this observation, a front velocity model was developed assuming rod-like irregularity structures (Wang & Morton, 2017). Alternatively, the anisotropy model assumes the irregularities to be ellipsoids, giving rise to diffraction patterns in the form of concentric ellipses (Fedor, 1967; Singleton, 1970). To solve for the anisotropy parameters and the drift velocity, the model uses information from receiver array autocorrelation functions in addition to cross-correlation functions (Armstrong & Coles, 1972; Rino & Livingston, 1982).

Space-time correlation schematic of the received signals can be a useful tool to analyze each correlation model. However, in the literature, it is only expressed in 2-D for some generic spatial dimension (Briggs et al., 1950; Kintner et al., 2004). In this study, the full space-time correlation schematics are constructed for the classic isotropy model, the front velocity model, and the anisotropy model. Based on the merits and drawbacks of each method, a hybrid correlation model is proposed. It first uses the anisotropy model to determine the drift velocity direction (and the orientation of the irregularities), and then it uses the front velocity model (with some adjustment) to determine the drift velocity magnitude. Using the hybrid correlation model, ionospheric irregularity drift velocity estimates are obtained from carrier phase measurements collected by a multi-GNSS receiver array at the Poker Flat Research Range, near Fairbanks, Alaska, during scintillation (Wang et al., 2018; Wang & Morton, 2017). To validate this model, the estimated irregularity drift velocities are cross compared against the measurements from the colocated all-sky imager (ASI) and the Poker Flat incoherent scatter radar (PFISR) during an intense geomagnetic storm event on 20 December 2015.

Although different correlation models make different assumptions on the shape of the diffraction pattern, all correlation models discussed in this study do share some common assumptions. First, the “frozen-in” assumption assumes minimal evolution in irregularity structure and drift direction within the correlation interval (Mitra, 1949). As a result, similar space-time correlation patterns can be observed at each receiver, allowing for an average drift velocity to be obtained. Second, the correlation functions are assumed to be strictly decreasing functions on both sides of the correlation peaks (Armstrong & Coles, 1972). Following this assumption, it is feasible to fully characterize the space-time correlation for each correlation model. And lastly, a geometric optics relationship is assumed between election density perturbation in the irregularity structure and the carrier phase fluctuation in the received signals (Rino & Fremouw, 1977; Rino & Livingston, 1982). This assumption establishes a unique relationship between the irregularity in space and the observed correlation pattern on the ground.

For nongeostationary satellites, the irregularity drift velocity in the ionosphere is not the same as the drift velocity of diffraction pattern observed on the ground, due to the effect of the satellite scan velocity (Kil et al., 2000). A detailed procedure for calculating the satellite scan velocity can be found in Wang and Morton (2015). An error analysis of the satellite scan velocity with respect to the irregularity height is given in Wang et al. (2018). In this study, we first place an emphasis on the diffraction pattern drift velocity when analyzing the correlation models. Then, the satellite scan velocity is added to the solution to obtain the irregularity drift when cross comparing against measurements from other instruments.

2. Correlation Models

2.1. Classic Isotropy Model

Once the time lag information has been obtained from cross correlation, 1-D apparent drifts along receiver pairs can be calculated based on the baseline distance between the pair of receiver antennas. To resolve the 2-D diffraction pattern drift velocity from these apparent drifts, a correlation model has been established with an implicit assumption that the observed correlation functions of the diffraction pattern are statistically isotropic (Briggs, 1968; Briggs et al., 1950; Mitra, 1949). Then it immediately follows that the diffraction patterns would take the form of concentric circles. In this paper, this model is referred to as the classic isotropy model. This model addresses a key issue on how to estimate the 1-D drift velocity components along a pair of receivers whose alignment is at an angle with respect to the diffraction pattern drift direction. This is illustrated by the following example: Let RX_1 and RX_2 represent the receiver pair location along the OX direction, where RX_1 is at the origin O. An isotropic diffraction pattern is drifting at velocity $\boldsymbol{V^D}$ at an angle θ to the OX axis. Let the corresponding time lag at the receiver pair cross-correlation peak be τ_0. Then, the apparent drift velocity between this pair of receivers along the OX direction is $\boldsymbol{V_x^A} = \xi_0/\tau_0$, where $\xi_0 = |RX_1 - RX_2|$. Figure 1 illustrates the geometry associated with this example.

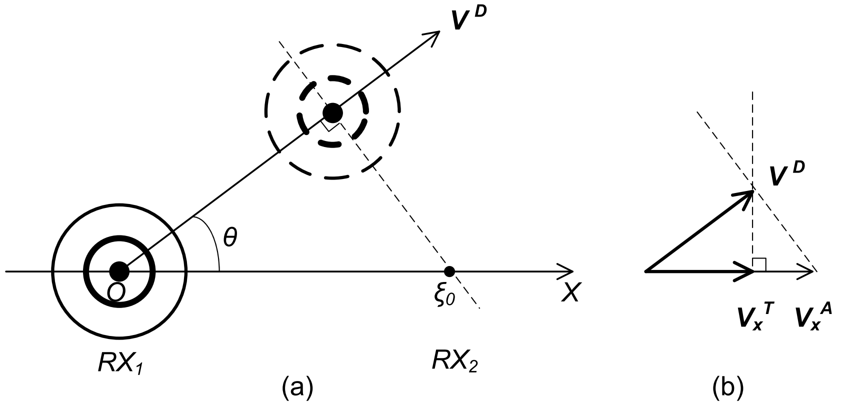

Figure 1. Illustration of the classic isotropy model. (a) The diffraction pattern is drifting at velocity $\boldsymbol{V^D}$ at an angle θ to the OX axis. The solid and dashed concentric circles indicate the observed correlation pattern caused by diffraction, where maximum correlations are observed τ_0 seconds apart at RX_1 and RX_2, respectively. (b) The velocities derived from this configuration.

Note that the concentric circles in subplot (a) are shown with different line widths, reflecting the monotonic decrease of the correlation functions. Subplot (b) shows the velocities derived from this configuration, where $\boldsymbol{V^D}$ represents the 2-D diffraction pattern drift and $\boldsymbol{V_x^A}$ is the 1-D apparent drift along the OX axis. As for $\boldsymbol{V_x^T}$, Briggs et al. (1950) define it as the true drift velocity along the receiver pair direction "with which an observer would have to move along OX in order to reduce the speed of fading as observed by him to a minimum". Indeed, an observer moving along the OX axis with velocity $\boldsymbol{V_x^T}$ would find the diffraction pattern fading most slowly in time, as the observer is always at the closest point on OX with respect to the diffraction pattern.

This is an intuitive definition under the isotropic assumption, as $\boldsymbol{V_x^T}$ would coincide with the velocity component of $\boldsymbol{V^D}$ along OX. If both $\boldsymbol{V_x^T}$ and $\boldsymbol{V_x^A}$ are known, the 2-D diffraction pattern drift can be reconstructed from these 1-D true drift velocities along receiver pairs using the following mathematical relations:

$$\boldsymbol{V_x^A} = \boldsymbol{V^D} / \cos\theta, \quad \boldsymbol{V_x^T} = \boldsymbol{V^D} \cos\theta \tag{1}$$

However, in reality, the diffraction pattern is expected to be anisotropic due to the high parallel conductivities of the ionosphere (Mendillo & Baumgardner, 1982). In this case, equation set (1) may not hold, since both the elongation and orientation of the anisotropic diffraction pattern would impact the projections of $\boldsymbol{V^D}$ onto the OX axis.

To account for the above ambiguity, it is more adequate to establish a generalized relationship between these velocities and the correlation functions of receiver array measurements. Briggs et al. (1950) proposed a space-time correlation schematic following the assumption of monotonically decreasing correlation functions. To construct the full space-time correlation schematic covering all spatial dimensions, it is helpful to understand the correlation surface along a single spatial dimension (Briggs et al., 1950; Kintner et al., 2004). For instance, using the above example, the space-time correlation surface characterizing the drift velocity components with respect to the correlation functions can be constructed. Figure 2 illustrates the resulting schematic along the spatial dimension defined by the OX axis, which is at an angle θ ($0^\circ < \theta < 90^\circ$) to the diffraction pattern drift.

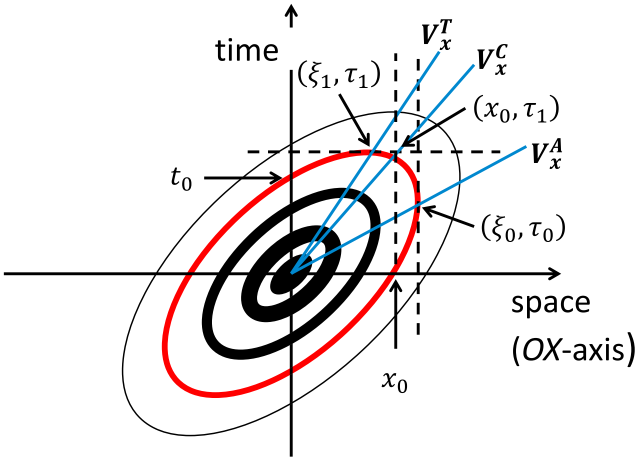

Figure 2. The space-time schematic along the OX axis, showing the correlation surface defined in Figure 1 for this spatial dimension. The concentric ellipses depict the correlation surface with monotonic decreasing values from the origin. The ellipse in red corresponds to correlation values equal to the cross-correlation peak of carrier phase measurements from the two receivers. It crosses the time axis at t_0 and the space axis at x_0. The blue lines give the drift velocity components, with $\boldsymbol{V_x^T}$ associated with displacement ξ_0 at time τ_0, $\boldsymbol{V_x^C}$ associated with x_0 at τ_1 and $\boldsymbol{V_x^A}$ associated with ξ_1 at τ_1.

In this space-time domain, different velocities are associated with various straight lines that go through the origin. Here the velocity is defined as displacement over time (ξ/τ). Hence, the inclination angles of the lines determine the magnitude of the velocity, where lower inclination angles correspond to larger velocities. In Figure 2, the vertical cut tangent to the red ellipse gives the cross correlation function, with its peak giving the apparent drift velocity $\boldsymbol{V_x^A}(=\xi_0/\tau_0)$. Also, the horizontal cut finds the true drift velocity $\boldsymbol{V_x^T}$ $(=\xi_1/\tau_1)$ at the slowest diffraction pattern fading in time, reflected by the slowest change in the correlation function. The relationship between these two velocities is given by the following equation (Kintner et al., 2004):

$$\boldsymbol{V_x^T} = \frac{1}{1+(t_0/\tau_0)^2}\boldsymbol{V_x^A} \tag{2}$$

where t_0 can also be understood as the time at which the autocorrelation function takes on the peak value of the cross-correlation function. While τ_0 is largely dependent on the inclination of the ellipses related to the drift velocity magnitude, t_0 is closely associated with the elongation of the ellipses. The ratio t_0/τ_0 determines the extent to which the apparent and true velocities are equivalent.

Briggs et al. (1950) also defined the characteristic velocity $\boldsymbol{V_x^C}$ as a measure of the fading rate of the diffraction pattern

$$\boldsymbol{V_x^C} = \frac{x_0}{\tau_1} = \frac{t_0/\tau_0}{1+(t_0/\tau_0)^2}\boldsymbol{V_x^A} \tag{3}$$

For some fixed τ_1 value, as x_0 decreases, the concentric ellipses become increasingly elongated. This leads to a faster rate of change in the correlation function, which implies larger diffraction pattern fading rate. From equations (2) and (3), when the ellipses are highly elongated ($t_0 \to 0$), then $t_0/\tau_0 \to 0$, causing $\boldsymbol{V_x^T}\to\boldsymbol{V_x^A}$ and $\boldsymbol{V_x^C}\to 0$.

All velocity components in this spatial dimension share the same subscripts $\boldsymbol{x}$, as they are defined with respect to the *OX* axis configuration in the previously mentioned example. These subscripts can be altered under different spatial dimensions or even omitted when the spatial dimension is unspecified.

Previous studies indicated that when receivers are placed along the same geomagnetic latitude in equatorial regions, $\boldsymbol{V^C}$ becomes significant only during periods of irregularity growth and is rather small during other times (Spatz et al., 1988; Vacchione et al., 1987). On this account, Kil et al. (2000) suggested that $\boldsymbol{V^T}$ may be approximated to $\boldsymbol{V^A}$ with errors of less than 10 m/s. Kintner et al. (2004) also showed support for this claim and demonstrated that the direction of equatorial drift is zonal in most cases. To summarize, when the receiver array placement and drift velocity are both zonal, that is, $\theta \approx 0^\circ$, it follows that $\boldsymbol{V^T} \approx \boldsymbol{V^A}$ and $\boldsymbol{V^C} \approx \boldsymbol{0}$.

The space-time correlation surface in the above example can serve as a useful tool for analyzing different correlation models. However, it can be very challenging to differentiate between two correlation models based on their correlation surfaces along a single spatial dimension. Therefore, it is necessary to construct their full space-time correlation schematics by assembling correlation surfaces in all spatial dimensions. In this study, using the classic isotropy model as an example, the space-time correlation schematic is constructed as the following.

First, space-time correlation surfaces are obtained along selected spatial dimensions for different θ values. This is performed for three diffraction pattern propagation scenarios: (a) parallel to the receiver pair orientation ($\theta = 0^\circ$), (b) perpendicular to the receiver pair orientation ($\theta = 90^\circ$), and (c) somewhere between (a) and (b) ($0^\circ < \theta < 90^\circ$). The corresponding spatial dimensions are denoted as (a) $\zeta_{||}$, (b) $\zeta_{\perp}$, and (c) ζ_θ. Then, with the first two extreme cases and the last general case, the full space-time correlation can be derived. The resulting individual correlation surfaces and the full space-time correlation schematic are shown in Figure 3.

In Figure 3, subplots (a)–(c) illustrate the correlation surfaces in red, green, and blue, under the three scenarios. Similar to Figure 1, the widths of the lines correspond to different correlation strengths. Along the $\zeta_{||}$, $\zeta_{\perp}$, and ζ_θ axes, the estimated true velocities are marked by the circles, while the apparent velocities are marked by the squares. In subplot (d), ζ_x-ζ_y represents the horizontal receiver plane defined by the user. For example, ζ_x can represent the geomagnetic east direction, while ζ_y can be the geomagnetic south. In the bottom figure, the gray cylinder represents the full space-time correlation for the classic isotropy model in the space-time

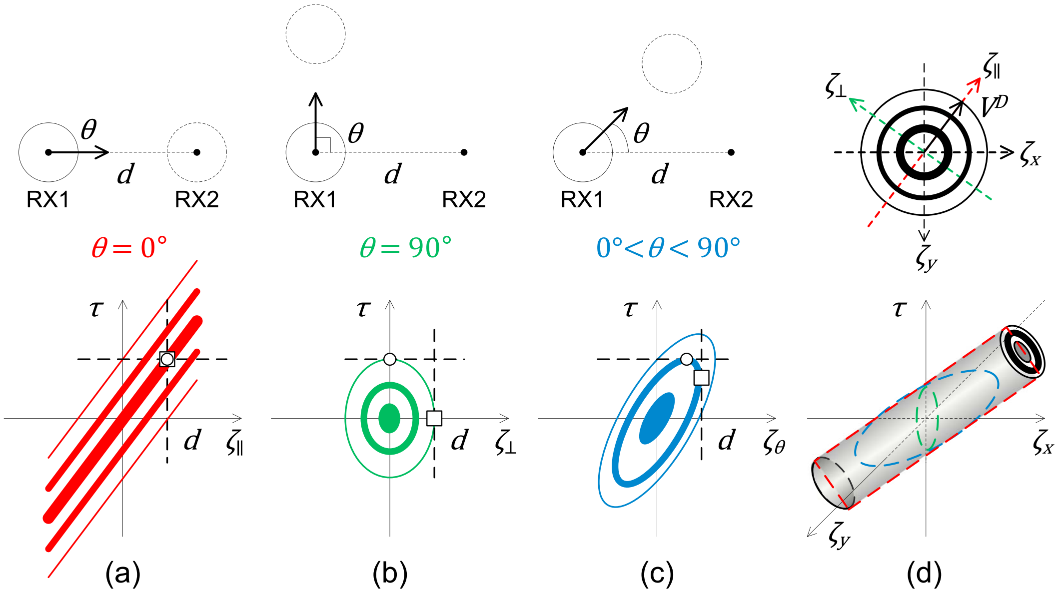

Figure 3. Individual space-time correlations along different spatial dimensions for (a) $\theta = 0^\circ$ in red, (b) $\theta = 90^\circ$ in green, and (c) $0^\circ < \theta < 90^\circ$ in blue, as well as the full space-time correlation schematic (d) for the classic isotropy model. For subplots (a)–(c), an illustration is given on top of the correlation pattern for each θ value, while $\zeta_{\parallel}$, $\zeta_{\perp}$, and ζ_{θ} are the corresponding spatial dimensions. d marks the distance between receivers RX_1 and RX_2; the square marks the apparent drift velocity, and the circle marks the true drift velocity. For subplot (d), the top row gives the horizontal cut through the ζ_x-ζ_y plane, showing the correlation pattern from diffraction as concentric circles. In the space-time schematic at the bottom, the dashed shapes mark the vertical cuts along each spatial dimension as in subplots (a)–(c).

domain defined by the ζ_x-ζ_y plane and the τ axis. The cross section at the top of the cylinder shows the correlation strengths through the concentric ellipses. The dashed shapes outline the intersections from the vertical cuts along each individual dimension for the three scenarios in red, green, and blue, respectively. The cylinder goes through the ζ_x-ζ_y plane at an inclination, which gives the magnitude of $\boldsymbol{V^D}$. A horizontal cut through the cylinder at $\tau = 0$ gives the spatial correlation pattern caused by diffraction. In the case of the classic isotropy model, the resulting cross section takes the shape of concentric circles. This is characterized by the top figure of subplot (d), while the black arrow along $\zeta_{\parallel}$ shows the direction of $\boldsymbol{V^D}$.

Along each spatial dimension in subplots (a)–(c), the apparent drift velocity (square) is obtained at the cross-correlation peak along the vertical cut of the correlation surface at the receiver distance. Then, tracing the correlation values same as the peak value, a horizontal cut determines the true drift (circle) following the definition by Briggs et al. (1950). In this example, the strict frozen-in assumption is applied that the correlation strength does not decrease over time within the correlation interval. Therefore, the true drift and the apparent drift are the same in subplot (a) when the diffraction pattern happens to be traveling along the receiver pair alignment. This agrees with the aforementioned observation from the literature. As θ increases, the true drift decreases in magnitude while the apparent drift increases (see subplot [c]). Eventually, when θ approaches 90°, the true drift becomes zero as the apparent drift approaches infinity (see subplot [b]).

Again, the main drawback of the classic isotropy model is that the isotropic assumption is not particularly realistic. In fact, ionospheric irregularity structures are expected to be anisotropic and highly elongated along magnetic field lines. This leads to rod-like diffraction patterns instead of circular ones. Another issue is that the definition of the true velocity can sometimes be ambiguous, as it may not equal to the projected velocity component of the 2-D diffraction pattern drift. Consequently, the reconstruction process via vector addition would be erroneous, over-estimating $\boldsymbol{V^D}$. This will be explained in the following sections.

2.2. Front Velocity Model

To better address the anisotropic nature of the ionospheric irregularities, Wang and Morton (2017) proposed a front velocity model designed for rod-like irregularities having larger footprints than the receiver array.

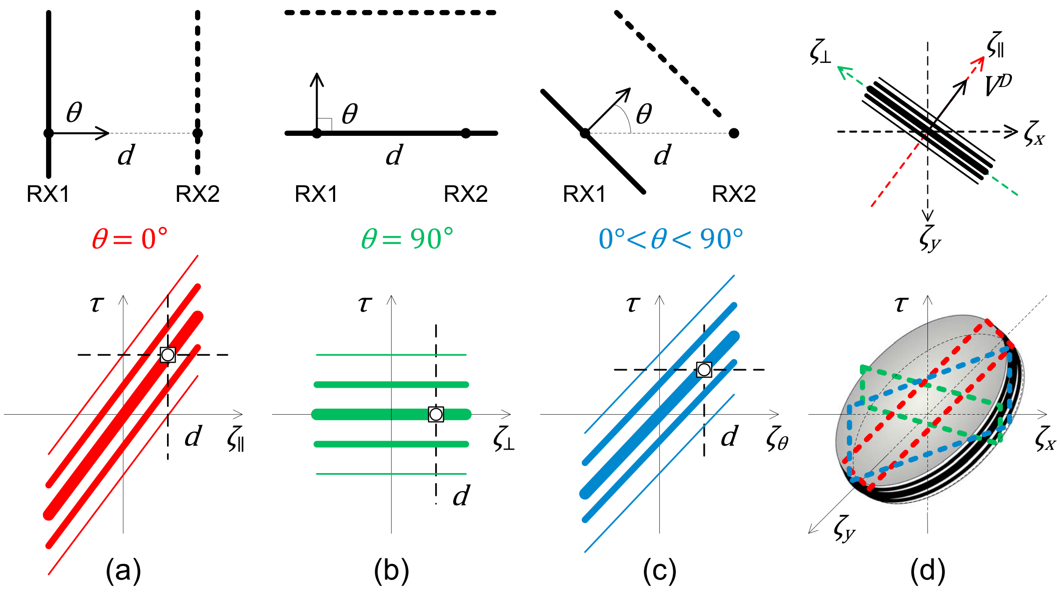

Figure 4. Space-time correlations along $\zeta_\parallel$ (a), $\zeta_\perp$ (b), and ζ_θ (c), as well as the full space-time correlation schematic for the front velocity model (d).

The method also assumes that the direction of the drift velocity is perpendicular to the velocity front (orientation of the diffraction pattern). This is a valid assumption under nominal conditions as the irregularity is aligned with the B field, and E × B drift is expected. Under these assumptions, the space-time correlation schematic is constructed for the front velocity model. The results are presented in Figure 4 following the rubrics of Figure 3.

In Figure 4, subplots (a)–(c) again give the correlation surfaces along the $\zeta_\parallel$, $\zeta_\perp$, and ζ_θ dimensions. Subplot (d) gives the space-time correlation as a disk, while the correlation strength is represented by the line width. Compared to Figure 3, major differences can be found in subplots (b) and (c). They can be understood as the extreme cases of Figures 3b and 3c as the diffraction pattern becomes increasingly anisotropic. Like the previous example, the strict frozen-in assumption is applied. As a result, subplot (a) is very similar to Figure 3 a. Again, a horizontal cut through the disk along the ζ_x-ζ_y plane gives the shape of the diffraction pattern, which is a rod-like pattern as in the top figure of subplot (d). Note that when finite rod length is assumed, disk-like space-time correlation pattern can be observed as in the bottom figure of subplot (d), whereas sheet-like correlation pattern can be observed for infinite rod length. Both scenarios would lead to the same diffraction pattern drift as long as the rod-like diffraction pattern has a larger footprint than the receiver array baseline.

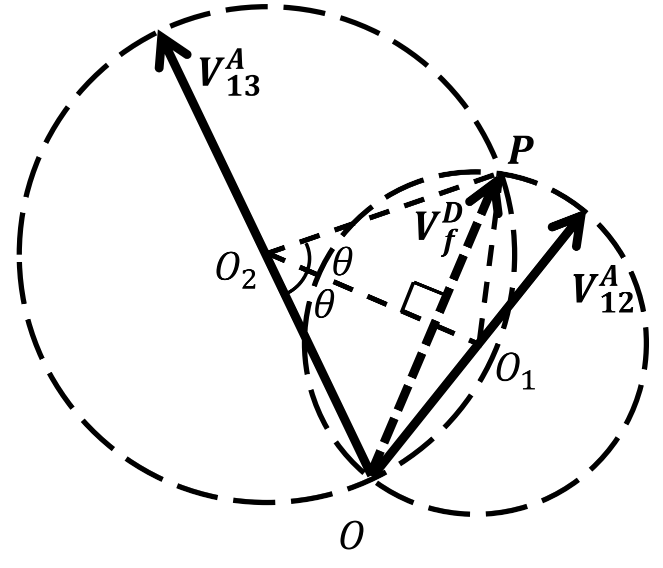

Figure 5. Illustration of the deterministic method for calculating the front velocity. V_{12}^A and V_{13}^A (solid arrows) are the apparent drifts along the receiver pairs, defining the dashed solution circles. The two circles intersect at point P, giving the solution to the diffraction pattern drift velocity V_f^D (dashed arrow). Points O_1 and O_2 are the center of the solution circles in the Cartesian coordinate system with O being the origin.

Unlike the classic isotropy model, the estimated apparent velocities and true velocities coincide in all spatial dimensions for the front velocity model. As a result, the true velocity as defined in the classic isotropy model does not reflect the velocity component of the 2-D diffraction pattern drift along ζ_x or ζ_y.

To resolve this issue, the front velocity model (and later the anisotropy model) directly calculates the true 2-D drift velocity vector, instead of attempting to resolve its x and y components. Wang and Morton (2017) provided a minimal mean square solution for an arbitrary GNSS array with n receivers, as well as a deterministic solution for a basic array of three receivers. The approach is to exploit the assumption that the drift velocity is perpendicular to the velocity front. This leads to potential solutions that lie on a circle corresponding to the receiver pair. With two or more of these solution circles, the 2-D drift can be determined at their intersection. Figure 5 illustrates the deterministic method for obtaining the front velocity for three receivers (RX_1, RX_2, and RX_3).

In Figure 5, $\boldsymbol{V}_{\boldsymbol{12}}^{\boldsymbol{A}}$ and $\boldsymbol{V}_{\boldsymbol{13}}^{\boldsymbol{A}}$ corresponds to the apparent drift velocities observed from receiver pairs RX_1-RX_2 and RX_1-RX_3, respectively. Since the front velocity is assumed to be perpendicular to the orientation of the rod-like irregularity, solution circles can be formed from $\boldsymbol{V}_{\boldsymbol{12}}^{\boldsymbol{A}}$ and $\boldsymbol{V}_{\boldsymbol{13}}^{\boldsymbol{A}}$. The intersection of the two circles gives the deterministic solution for the diffraction pattern drift $\boldsymbol{V}_{\boldsymbol{f}}^{\boldsymbol{D}}$ under the front velocity model. Let the origin of this system be $O(0, 0)$, and let the centers of the circles be $O_1(x_1, y_1)$ and $O_2(x_2, y_2)$. To solve for $\boldsymbol{V}_{\boldsymbol{f}}^{\boldsymbol{D}} = P(x, y)$, note that (1) ΔPO_2O_1 and ΔOO_2O_1 are congruent triangles ($\Delta PO_2O_1 \cong \Delta OO_2O_1$); hence, $\angle PO_2O_1 = \angle OO_2O_1 = \theta$; 2) $PO \perp O_2O_1$. By applying dot-product and trigonometry properties to these observations, a unique solution for $P(x, y)$ can be obtained

$$x = 2r_2^2 \sin^2\theta \frac{y_1 - y_2}{x_2y_1 - x_1y_2} \tag{4}$$

$$y = 2r_2^2 \sin^2\theta \frac{x_2 - x_1}{x_2y_1 - x_1y_2} \tag{5}$$

For a receiver array with $n \geq 3$ receivers, this system is overdetermined. There are $\binom{n}{2}$ such solutions, which can be used to create more robust drift velocity estimates.

It should be noted that due to the inverse relationship between time lag and velocity, any error in time lag measurements can lead to large velocity errors when the time lag value is small. To address this, the algorithm adaptively rejects receiver pair cross-correlation peaks that are associated with the smaller time lag values. This effectively produces more reliable drift velocity magnitude estimates.

The drawback of the front velocity model is inherited from the perpendicular assumption between the velocity front and drift direction. This assumption is suitable for equatorial regions (Ji et al., 2011). However, it becomes less viable under active geomagnetic conditions, especially at high latitudes, where interplanetary magnetic field and auroral electrojet also play important roles in the direction and magnitude of the drift velocity.

2.3. Anisotropy Model

The anisotropy model is developed to address the more realistic anisotropic nature of the diffraction pattern induced by ionospheric scintillation (Fedor, 1967). The model consists of two parts, the forward propagation model and the correlation model. The forward propagation model projects the ionospheric irregularities in space to the diffraction pattern on the receiver plane (Singleton, 1970). The correlation model estimates the anisotropy parameters and diffraction pattern drift velocity from receiver array measurements (Armstrong & Coles, 1972). It assumes that the space-time correlation caused by the diffraction pattern takes the form of concentric ellipsoids (Rino & Livingston, 1982). The focus of this section is on the correlation model, while a detailed description of the forward propagation model can be found in Rino and Fremouw (1977).

Unlike the cases for the classic isotropy model and the front velocity model, a less strict frozen-in assumption is applied for the anisotropy model by allowing small decrease in the correlation strength within the correlation interval. This adaptation is necessary for the space-time correlation to remain consistent with the “concentric ellipsoids” assumption made by the anisotropy model. The resulting space-time correlation schematic of the anisotropy model is shown in Figure 6.

In Figure 6, subplots (a)–(c) again illustrate the correlation surfaces for the spatial dimensions $\zeta_{||}$, $\zeta_{\perp}$, and ζ_{θ}, while subplot (d) gives the outline of the space-time correlation as an ellipsoid. In addition, b' and a' mark the intersections between the x and y axes with a common correlation ellipsoid in subplots (a) and (b), giving the axial ratio ($a^{'} : b^{'}$) of the diffraction pattern. Note that subplot (a) is different from those of Figures 3a and 4a; instead of straight lines of correlation values, highly elongated concentric ellipses are obtained. This is a direct corollary of the concentric ellipsoids assumption. Although subplots (b) and (c) are very similar to Figures 3b and 3c in the classic isotropy model, subplot (d) is closer to Figure 4d in the front velocity

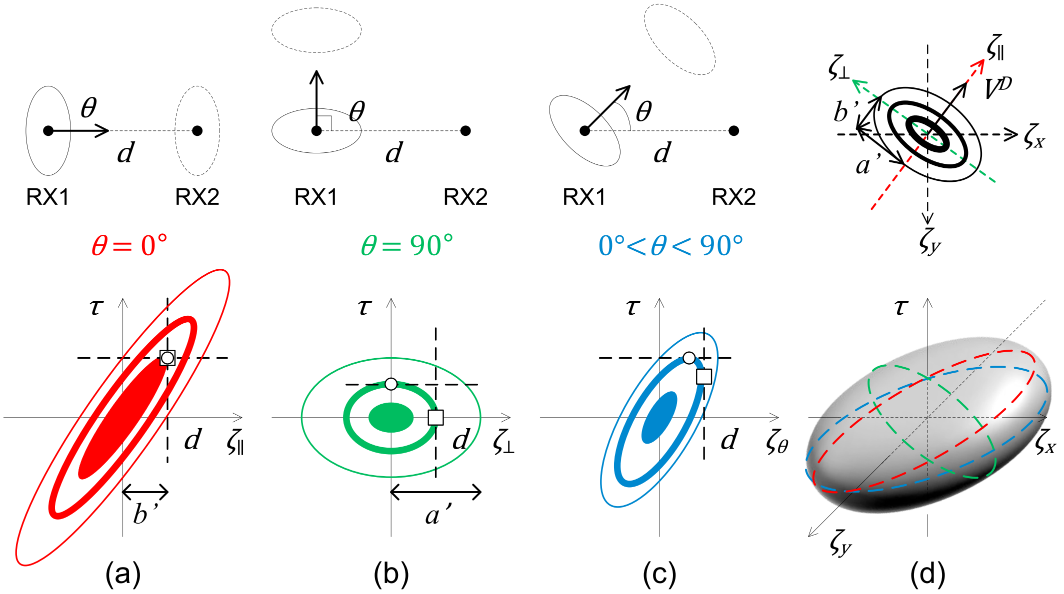

Figure 6. Space-time correlations along $\zeta_{\|}$ (a), $\zeta_{\perp}$ (b), and ζ_{θ} (c), as well as the full space-time correlation schematic for the anisotropy model (d). a' and b' are scaled semimajor and semiminor axes of the diffraction pattern.

model. This is an expected outcome when the axial ratio of the diffraction pattern is large ($a' \gg b'$). In equatorial studies, large axial ratio values are regularly observed (Kintner et al., 2004). Also, large axial ratio assumptions of $a' : b' \geq 50$ are often used in scintillation modeling (Carrano et al., 2016; Secan et al., 1995).

Compared to the isotropy and front models, the anisotropy model is more complex and requires information from the autocorrelation function in addition to cross-correlation functions to solve for the anisotropy. In essence, a space-time correlation ellipsoid of constant correlation magnitude can be modeled by a set of anisotropy parameters (a', b', ψ, $|v|$, θ), where $a' : b'$ gives the axial ratio of the diffraction pattern, the angle ψ depicts the orientation of the diffraction pattern, $|v|$ is the magnitude of the correlation and the angle θ gives the drift direction.

There are two general methods for solving these anisotropy parameters. The first method, developed based on Fedor (1967), focuses on points in autocorrelation and cross-correlation functions with the same correlation value. These points can be associated with a common space-time correlation ellipsoid. Therefore, the anisotropy parameter set (a', b', ψ, $|v|$, θ) can be solved simultaneously in one step. A recent refinement of this approach is described in Su et al. (2017). The second method, developed based on Armstrong and Coles (1972), focuses on intersections between correlation functions. These intersections have the same τ values and can be associated with the same horizontal cut of the space-time correlation ellipsoid. Effectively, this method takes a two-step approach. It first solves for the diffraction pattern parameters (a', b', ψ) based on the correlation intersections with additional information at the cross-correlation peaks. It then uses the solution to find the drift velocity parameters ($|v|$, θ). Figure 7 gives an example showing the different data points used in the one-step approach against the two-step approach.

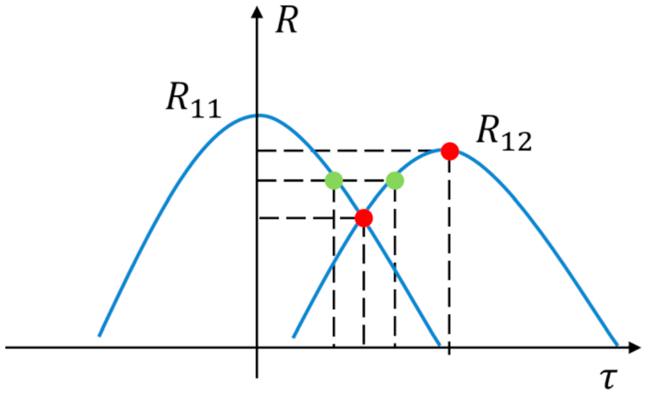

Figure 7. Illustration of data points used in the one-step approach (green) and the two-step approach (red) for solving the anisotropy. R_{11} and R_{12} represent the autocorrelation and cross-correlation functions obtained from the receiver pair (RX_1 and RX_2) measurements.

In Figure 7, the two green dots represent points on R_{11} and R_{12} at the same correlation value used in the one-step approach. The two red dots represent the intersection between R_{11} and R_{12} and the cross-correlation peak used in the two-step approach. Comparable performances have been observed between these two methods (Costa et al., 1988; Khudukon

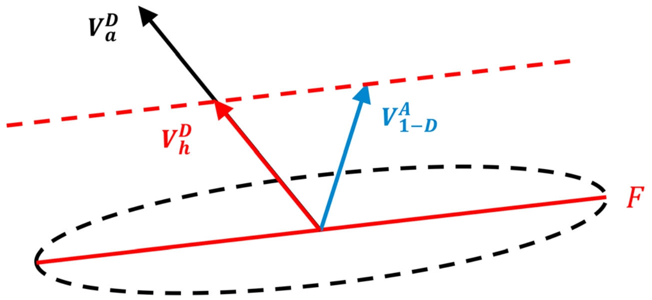

Figure 8. Illustration of the projection geometry for hybrid velocity estimation. $\boldsymbol{V_h^D}$ is the hybrid diffraction pattern drift projected from the 1-D apparent drift $\boldsymbol{V_{1-D}^A}$ onto the direction of the anisotropy drift $\boldsymbol{V_a^D}$ guided by the velocity front F. The dashed black ellipse is the solved anisotropy, while the red lines represent the velocity front orientation F.

et al., 1994). This study follows the two-step approach, refined based on the work of Rino and Livingston (1982). Details of the method are documented in the appendix.

As the estimated axial ratio approaches unity ($a^{'} : b^{'} \approx 1$), the diffraction pattern becomes nearly isotropic rather than anisotropic. This means that the diffraction patterns would be very similar when observed from different angles, making it very challenging to determine the orientation of the anisotropy. As a result, small axial ratios carry small confidence levels into the estimated anisotropy parameters. In practice, results associated with small axial ratios ($a^{'} : b^{'} < 2$) are excluded.

Another practical weakness of the anisotropy model is that it tends to overestimate the magnitude of the 2-D drift. An example is given later to demonstrate this problem using real data. Unlike the front velocity model, the anisotropy model cannot simply reject receiver estimates that are associated with small time lag values, since dropping correlation functions would quickly lead to an underdetermined system.

2.4. Hybrid Correlation Model

Based on the merits and drawbacks of each correlation method from the analysis above, a hybrid correlation method is proposed. First, the drift velocity direction and the diffraction pattern orientation are obtained using the anisotropy model. Then, taking these parameters as a priori, an adjusted front velocity model is created. It calculates the projection of the apparent velocity onto the drift direction along the diffraction pattern orientation as the velocity front. Following the adaptive filtering scheme of the front velocity model, measurements associated with smaller time lag values are then rejected. The remaining measurements are averaged to produce the final estimate of the 2-D diffraction pattern drift.

For example, in the Cartesian plane representing the velocity values, let the apparent 1-D diffraction pattern drift be $\boldsymbol{V_{1-D}^A} = (x_{1-D}, y_{1-D})$ along some arbitrary receiver pair. Say the anisotropy model finds the diffraction pattern drift velocity to be $\boldsymbol{V_a^D} = (x_a, y_a)$ and the velocity front orientation to be $F = (x_f, y_f)$. Then, the hybrid diffraction pattern drift velocity is $\boldsymbol{V_h^D} = (x_h, y_h)$ determined as a nonorthogonal projection of $\boldsymbol{V_{1-D}^A}$ onto $\boldsymbol{V_a^D}$ following the orientation of F. Figure 8 illustrates the projection geometry.

Based on Figure 8, the hybrid velocity can be determined as

$$x = \frac{y_{1-D} - k_f x_{1-D}}{k_a - k_f}, y = k_\mathrm{a} x \tag{6}$$

where $k_\mathrm{a} = y_a/x_a$ and $k_\mathrm{f} = y_f/x_f$ represent the gradients of the anisotropy drift and the velocity front, respectively. In the case where anisotropy parameters are not measurable, the final 2-D drift estimate takes the front velocity model solution if available.

3. Results and Analysis

A case study is conducted based on an intense geomagnetic storm event that occurred on 19 December 2015 and lasted until 21 December 2015. The particular data set used in this study is from 20 December 2015, when the geomagnetic disturbances were most intense. The global *Kp* index stayed above 4 throughout the day and reached 7+ at its peak, while the *Dst* index reached maximum intensity at −155 nT (World Data Center for Geomagnetism, Kyoto, http://wdc.kugi.kyoto-u.ac.jp/wdc/Sec3.html). The Auroral Electroject (*AE*) index also showed large disturbances and reached 1,883 nT at its maximum intensity (OMNIWeb service, http://omniweb.gsfc.nasa.gov/index.html). Moreover, the local magnetometer at Poker Flat, Alaska, observed large disturbances with approximately ±1,000 nT in the horizontal component and ±500 nT in the vertical measurements (UAF Alaska Satellite Facility, https://www.asf.alaska.edu/magnetometer). More details of this event are described in Wang and Morton (2017) and Wang et al. (2018).

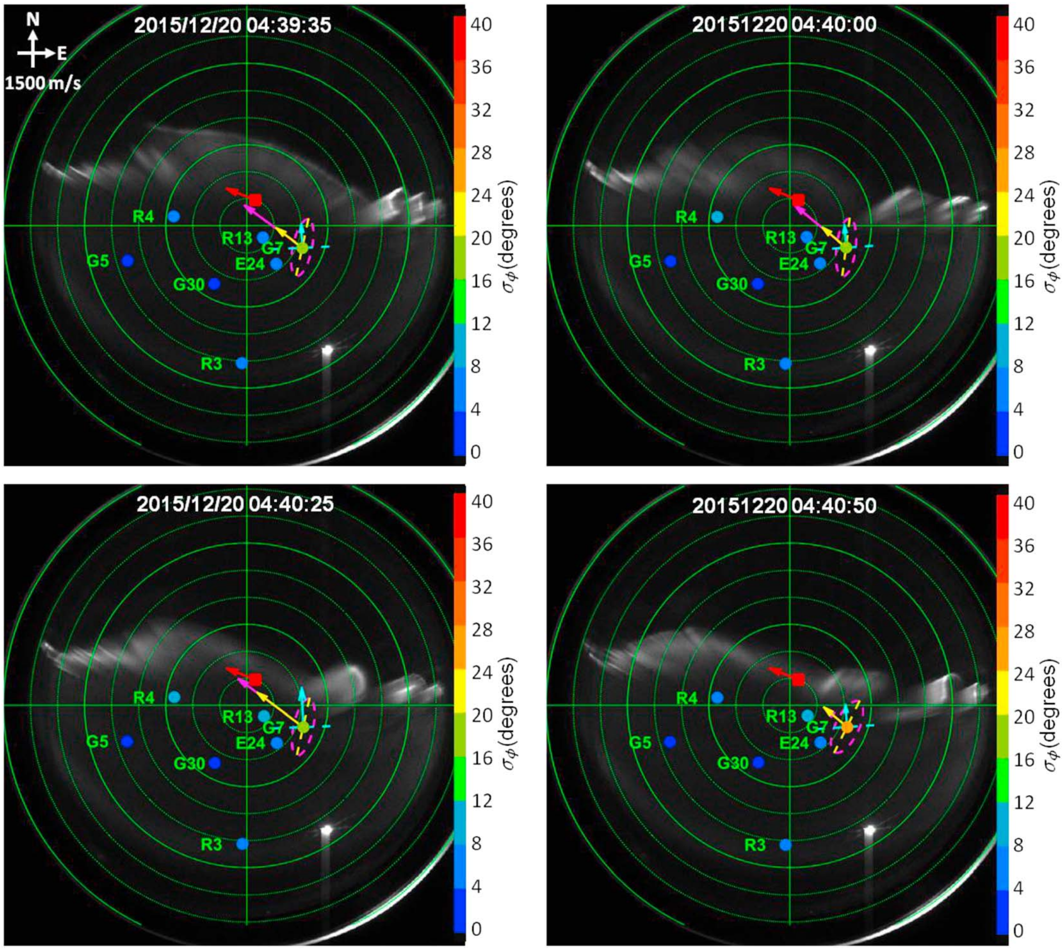

Figure 9. Cross comparison between drift velocity estimates from different correlation methods versus Poker Flat incoherent scatter radar (PFISR) vector velocity measurements on top of 557.7-nm ASI images from 04:30:25 to 04:31:40 UT on 20 December 2015. In each subplot, the red square and quiver represent the approximated PFISR beam center and the averaged PFISR vector velocity measurement, respectively. Global Navigation Satellite System satellites are plotted as dots with respect their elevation and azimuth angles using three-letter initials for abbreviation (G = GPS, R = GLONASS, E = Galileo). The color of each dot corresponds to the phase scintillation strength observed for each satellite, shown by the color bar. Drift velocity estimates for GPS PRN 7 from different correlation methods are given by the colored quivers (pink = anisotropy model, cyan = front velocity model, and yellow = hybrid model). The estimated topologies of these models are provided using dashed lines in the same colors. Geodetic reference velocity vectors at 1,500 m/s are given in white in the first subplot.

Ionospheric irregularity drift velocities are estimated based on the diffraction pattern drift from the proposed hybrid correlation model, together with the satellite scan velocity estimates. Velocities from the front velocity model and the anisotropy model are also calculated for comparison. These velocity estimates are cross compared against measurements from the on-site ASI and the PFISR adopting the comparison scheme used in previous studies (Wang et al., 2018; Wang & Morton, 2017). An elevation angle mask of 35° is applied to minimize the multipath effects. Figure 9 shows the comparison results using the geodetic coordinate system for four consecutive epochs from 04:39:35 UT with a 25-s interval.

In Figure 9, the PFISR beam center is approximated from the four PFISR beams used in this experiment: (14° az, 90° el), (−154.3° az, 77.5° el), (−34.7° az, 66.1° el), and (75° az, 65.6° el; Marigal Database, http://isr.sri.com/madrigal/). The PFISR velocity is averaged from measurements within (66°N, 66.75°N) geomagnetic latitudes, where most consistent results are observed. The PFISR velocity stays the same for all four subplots, as this 100-s period is within a 5-min PFISR data interval. A horizontal arc structure can be observed in the ASI images showing auroral emission. With closer examinations, the arc structure can be seen moving

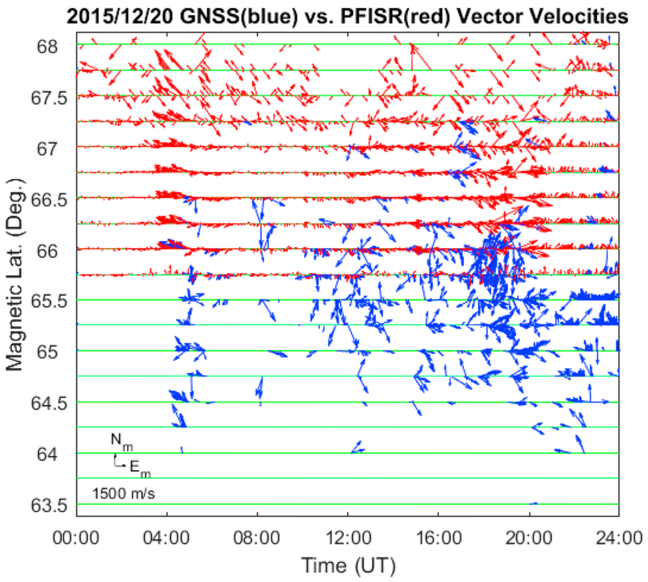

Figure 10. Cross comparison between the GNSS estimated irregularity drift velocities (blue) from the hybrid model against PFISR vector velocity measurements (red) on 20 December 2015. Reference vectors at 1,500 m/s pointing eastward and northward are given at the bottom left of the figure. PFISR = Poker Flat incoherent scatter radar.

westward during the 100-second observation period. This agrees with PFISR's vector velocity measurements. Meanwhile, good spatial associations can be observed between phase scintillations experienced on GNSS satellites and auroral emissions seen on ASI. Phase scintillation strengths that are above nominal values ($\sigma_\psi > 4^\circ$) are only observed on satellites closest to the irregularity: GPS 7, GLONASS 4, and GLONASS 13. Moderate scintillation is observed on GPS 7, producing measureable space-time correlations for drift velocity estimation.

For the front velocity model, the magnitude of the drift velocity estimates matches well against PFISR's measurement. But the orientation of the velocity front and the direction of the drift do not match with the local B field topology, whose declination angle was around 18.5°N (Thébault et al., 2015). For the anisotropy model, as shown by the dashed ellipses, the anisotropy orientation matches the B field orientation. Also, the directions of the estimated drift velocities agree with the PFISR results. However, the magnitudes of the velocity estimates are much larger than the PFISR measurements in the first three subplots. Combining the advantages of the front velocity model and the anisotropy model, the hybrid correlation model shows improved agreement with PFISR measurements, in both velocity magnitude and drift direction estimation.

Following the projection scheme from the geodetic coordinate system into geomagnetic, irregularity drift velocities are projected onto PFISR's field of view into different geomagnetic latitude bins (Wang et al., 2018). Figure 10 shows the cross-comparison results between GNSS drift velocity estimates from the hybrid model versus vector velocity measurements obtained by PFISR. While Figure 9 gives snapshots of individual scintillation events, Figure 10 depicts the temporal and spatial patterns of the irregularities over the entire day of 20 December 2015.

In Figure 10, the PFISR measurements are most consistent from 66°N to 66.75°N. Three common features can be identified across these geomagnetic latitudes. First, at around 0400 UT, large north-westward velocity components can be observed and quickly transitioned into small south-westward components. Second, from ~1500 to ~2100 UT, south-eastward drifts persisted with relatively large variations. Finally, from ~2100 to 2400 UT, small northward components emerged. These features can also be observed in GNSS-estimated results. Additionally, the GNSS results showed some large fluctuations post 1200 UT toward lower magnetic latitudes. In fact, the timing of these fluctuations corresponds well with a substorm that occurred from ~1200 to ~1400 UT (Wang & Morton, 2017). This substorm was localized toward the southern half of the sky outside of PFISR's limited observation volume, supported by ASI summary plots (Wang et al., 2018).

As can be observed from Figure 10, the GNSS array and PFISR have distinct spatial coverages and limited overlaps in their fields of view (detailed coverages of both systems can be found in Wang & Morton, 2017). Therefore, it is more suitable to analyze the overall statistical behaviors of the two systems. To that end, a quantitative comparison is carried out by investigating the mean values and standard deviations of PFISR's measurements and the combined velocity estimates from the GNSS receiver array. For the GNSS estimates, the results are binned into 5-min intervals to match with the PFISR's measurements from the original 25-s resolution. The results are shown in Figure 11.

Figure 11 once more indicates that the results from the GNSS array and PFISR are in good agreement. Comparing the mean values, in the east-west direction, the GNSS estimates are reasonably close to the PFISR measurements and are almost always within PFIRS's error bar boundaries. In the north-south direction, the agreement is slightly inferior. This is likely due to the shorter baseline separations in the north-south direction, as well as the possible error that occurred during coordinate transformation from geodetic to geomagnetic without knowledge of the vertical velocity component. The error bars of the GNSS array are also larger in the north-south direction, showing greater velocity variations. The dominant contribution to the GNSS velocity variations is likely to come from the spatial and temporal variations of the irregularity structures.

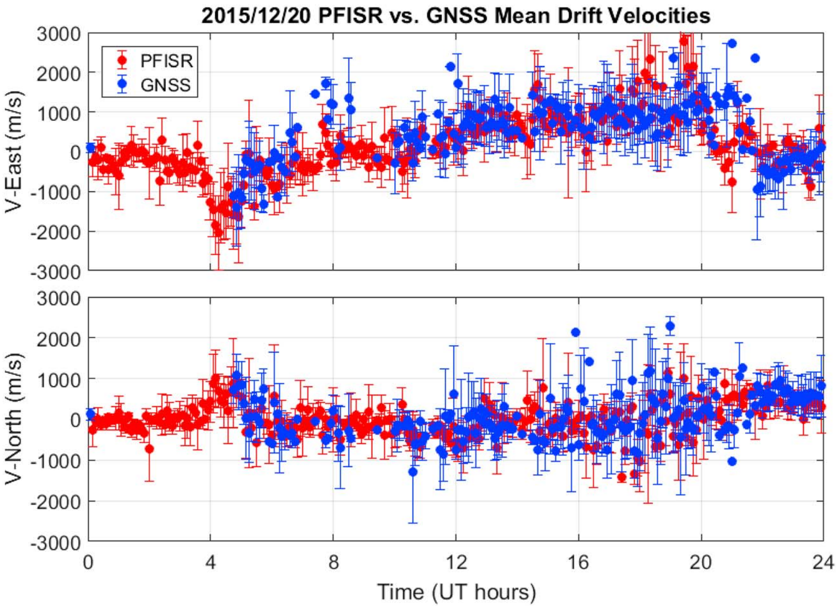

Figure 11. Cross comparison of mean drift velocities between the PFISR (red dots) and the GNSS array (blue dots) on 20 December 2015, together with their standard deviations as error bars. PFISR = Poker Flat incoherent scatter radar.

The last cross comparison is on the distribution of the velocity magnitudes. Note that this comparison only focuses on the results from 1000 to 2400 UT, as both the GNSS array and the PFISR have near-continuous data. Figure 12 shows the results.

In Figure 12, a general agreement can be seen between the two distributions. The PFISR distribution has a more distinct peak between velocities ranging from 400 to 800 m/s, while the GNSS distribution shows more proportion toward velocities above 1,300 m/s.

The above quantitative analyses are focused on the results estimated by the hybrid method. Similar studies are reproduced using both the front velocity model and the anisotropy model. To summarize the comparison results, the root-mean-square (RMS) values of the difference in mean velocity magnitude and orientation between GNSS array and PFISR are provided in the following table for the front velocity, anisotropy, and hybrid models.

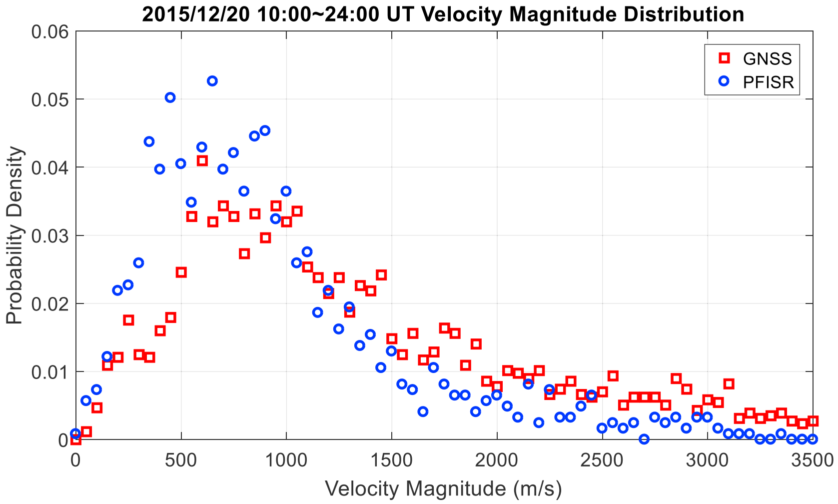

Figure 12. Cross comparison of the velocity magnitude distributions of the PFISR measurements (red squares) and the GNSS estimates (blue circles) between 1000 and 2400 UT on 20 December 2015. PFISR = Poker Flat incoherent scatter radar.

Table 1
RMS Values of GNSS Versus PFISR for all Three Correlation Models on 20 December 2015

Correlation models	RMS V-east (m/s)	RMS V-north (m/s)	RMS magnitude (m/s)	RMS angle (rad)
Front velocity	697.0	700.3	509.2	1.113
Anisotropy	1153.6	878.8	987.3	0.902
Hybrid	662.3	710.6	492.7	0.947

Note. RMS = root-mean-square; PFISR = Poker Flat incoherent scatter radar.

As can be seen in Table 1, the front velocity model has RMS velocity values comparable to the hybrid model. However, it has the largest RMS angles. On the contrary, the anisotropy model produces the smallest RMS angle values but tends to overestimate the velocity values. In this example, the hybrid method demonstrates the best overall performance among the three correlation models.

4. Conclusion

In the context of spaced-receiver studies for irregularity drift velocity estimation, this study focuses on the correlation analysis of the received diffraction pattern. Three correlation models are analyzed in detail through their space-time correlation schematics, including the classic isotropy model, the front velocity model, and the anisotropy model. Based on the merits and drawbacks of each method, a hybrid correlation model is proposed combining the anisotropy model and the front velocity model. Drift direction and diffraction pattern orientation are first obtained from the anisotropy model. Drift magnitude is then determined via the adjusted front velocity model taking the diffraction pattern orientation as the velocity front. As shown in a real-data example, the hybrid correlation model exhibits superior performance over the prevalent models.

Through a case study of a geomagnetic storm event on 20 December 2015, the GNSS-estimated drift velocities using the hybrid correlation model are cross compared with measurements from both the ASI and the PFISR. The comparison results are favorable in several aspects, including direction and magnitude of the drift motion, orientation of the irregularity, detailed temporal and spatial features, averaged behaviors over time, as well as the statistical distribution of the drift velocity magnitude. Similar analyses are conducted for the front velocity and anisotropy models. The RMS values of GNSS versus PFISR suggest that the hybrid model has the best overall performance. In the future, more case studies from both high-latitude and equatorial regions will be analyzed to further validate this hybrid correlation method.

Appendix A: Anisotropy Parameters Estimation

Following Rino and Livingston (1982), the diffraction pattern caused by the propagated anisotropic irregularity structure is characterized by the quadratic function

$$f^2(\Delta\boldsymbol{\rho}_s) = \frac{C\Delta\rho_{s_x}^2 - B\Delta\rho_{s_x}\Delta\rho_{s_y} + A\Delta\rho_{s_x}^2}{AC - B^2/4} \tag{A1}$$

where $\Delta\rho_{s_x}$ and $\Delta\rho_{s_y}$ are the receiver displacement along the x axis and y axis. A, B, and C are the anisotropy parameters to represent the shape of the ellipse. It is more convenient to rewrite equation (A1) in matrix form

$$f^2(\Delta\boldsymbol{\rho}_s) = \Delta\boldsymbol{\rho}_s{}^T \mathscr{E} \Delta\boldsymbol{\rho}_s \tag{A2}$$

where $\mathscr{E}$ is a 2×2 matrix

$$\mathscr{E} = \frac{1}{AC - B^2/4}\begin{bmatrix} C & -B/2 \\ -B/2 & A \end{bmatrix} \tag{A3}$$

For a system of n spaced receivers, the total number of correlation functions is n^2. Denote each correlation function as $R_{ij}(\Delta t)$, where i and j represent specific receiver pairs with $i, j = 1, 2, \ldots, n$. This includes both autocorrelation functions ($i = j$) and cross-correlation functions ($i \neq j$). Based on the model described in the previous section, these correlation functions will take the general form

$$R_{ij}(\Delta t) = R_{ij}\left[f\left(\Delta\boldsymbol{\rho}_{ij} - \boldsymbol{V}^{\boldsymbol{D}}\Delta t\right); \Delta t\right] \tag{A4}$$

In the next step, these correlation functions are paired with each other to reveal more information about the anisotropy. For the convenience of problem formulation, the n^2 correlation functions are indexed consecutively from 1 to n^2 based on cardinality. For example, the autocorrelation function R_{11} is now labeled as R^1, and the cross-correlation function R_{13} is now labeled as R^3. Then equation (A4) can be rewritten as the following form using a single superscript notation

$$R^i(\Delta t) = R\left[f\left(\Delta\boldsymbol{\rho}^{(i)} - \boldsymbol{V}^{\boldsymbol{D}}\Delta t\right); \Delta t\right] \tag{A5}$$

where i takes the values from 1 to n^2.

Following the method of Armstrong and Coles (1972), the intercept time delay τ_{jk} between any pair of correlation functions is identified by

$$R\left[f\left(\Delta\boldsymbol{\rho}^{(j)} - \boldsymbol{V}^{\boldsymbol{D}}\tau_{jk}\right); \tau_{jk}\right] = R\left[f\left(\Delta\boldsymbol{\rho}^{(k)} - \boldsymbol{V}^{\boldsymbol{D}}\tau_{jk}\right); \tau_{jk}\right] \tag{A6}$$

By using the same matrix notation used in the previous section, it follows that equation (A5) holds only if

$$\left(\Delta\boldsymbol{\rho}^{(j)} - \boldsymbol{V}^{\boldsymbol{D}}\tau_{jk}\right)^T \mathscr{E}\left(\Delta\boldsymbol{\rho}^{(j)} - \boldsymbol{V}^{\boldsymbol{D}}\tau_{jk}\right) = \left(\Delta\boldsymbol{\rho}^{(k)} - \boldsymbol{V}^{\boldsymbol{D}}\tau_{jk}\right)^T \mathscr{E}\left(\Delta\boldsymbol{\rho}^{(k)} - \boldsymbol{V}^{\boldsymbol{D}}\tau_{jk}\right) \tag{A7}$$

or

$$\boldsymbol{V}^{\boldsymbol{D}^T}\mathscr{E}\left(\Delta\boldsymbol{\rho}^{(j)} - \Delta\boldsymbol{\rho}^{(k)}\right) = \frac{1}{2\tau_{jk}}\left[\Delta\boldsymbol{\rho}^{(j)T}\mathscr{E}\Delta\boldsymbol{\rho}^{(j)} - \Delta\boldsymbol{\rho}^{(k)T}\mathscr{E}\Delta\boldsymbol{\rho}^{(k)}\right] \tag{A8}$$

If $\mathscr{E}$,the anisotropy term is known, then the above equation constitutes an overdetermined system while $\boldsymbol{V}^{\boldsymbol{D}}$ can be solved using the least squares method (Armstrong & Coles, 1972; Rino & Livingston, 1982).

In order to determine the anisotropy parameters, another set of equations are introduced by considering the time lag τ_i produced when the correlation between a receiver pair is at maximum, including autocorrelation with the receiver itself, which leads to $\tau_i = 0$. Note that for a cross correlation, τ_i is exactly the time lag used to determine the apparent velocity in the previous sections. By direct computation under the frozen-in assumption, Rino and Livingston (1982) showed that τ_i must satisfy the relation

$$\boldsymbol{V}^{\boldsymbol{D}^T}\mathscr{E}\Delta\boldsymbol{\rho}^{(i)} = \tau_i\boldsymbol{V}_{\mathbf{eff}}^2 \tag{A9}$$

where

$$\boldsymbol{V}_{\mathbf{eff}} = f\left(\boldsymbol{V}^{\boldsymbol{D}}\right) = \left(\frac{C\boldsymbol{V}_{\boldsymbol{x}}^{\boldsymbol{D}}2 - B\boldsymbol{V}_{\boldsymbol{x}}^{\boldsymbol{D}}\boldsymbol{V}_{\boldsymbol{y}}^{\boldsymbol{D}} + A\boldsymbol{V}_{\boldsymbol{y}}^{\boldsymbol{D}}2}{AC - B^2/4}\right)^{1/2} \tag{A-10}$$

By substituting equation (A9) into equation (A8), there is

$$\Delta\boldsymbol{\rho}^{(j)T}\left[\mathscr{E}/\boldsymbol{V}_{\mathbf{eff}}^2\right]\Delta\boldsymbol{\rho}^{(j)} - \Delta\boldsymbol{\rho}^{(k)T}\left[\mathscr{E}/\boldsymbol{V}_{\mathbf{eff}}^2\right]\Delta\boldsymbol{\rho}^{(k)} = 2\tau_{jk}\left(\tau_j - \tau_k\right) \tag{A11}$$

This system of equation is in general overdetermined, hence can be used to solve for $\left[\mathscr{E}/\boldsymbol{V}_{\mathbf{eff}}^2\right]$ using least squares. Moreover, knowing $\left[\mathscr{E}/\boldsymbol{V}_{\mathbf{eff}}^2\right]$ is sufficient to determine $\boldsymbol{V}^{\boldsymbol{D}}$ in the system of equations described by equation (A9), as we can simply divide both sides by an arbitrary $\boldsymbol{V}_{\mathbf{eff}}^2$ to turn $\mathscr{E}$ into $\left[\mathscr{E}/\boldsymbol{V}_{\mathbf{eff}}^2\right]$.

To better formulate the system of equations into a least squares problem, equation (A11) is rewritten in a more compact form by defining the $N_I \times 3$ matrix

$$\mathscr{D} = \begin{bmatrix} D_{xx}^{(1)} & D_{xy}^{(1)} & D_{yy}^{(1)} \\ \vdots & \vdots & \vdots \\ D_{xx}^{(N_I)} & D_{xy}^{(N_I)} & D_{yy}^{(N_I)} \end{bmatrix} \tag{A12}$$

with the elements

$$D_{xx}^{(i)} = \Delta\rho_x^{(j)}2 - \Delta\rho_x^{(k)}2 \tag{A13}$$

$$D_{xy}^{(i)} = \Delta\rho_x^{(k)}\Delta\rho_y^{(j)} - \Delta\rho_x^{(j)}\Delta\rho_y^{(k)} \tag{A14}$$

$$D_{yy}^{(i)} = \Delta\rho_y^{(j)}2 - \Delta\rho_y^{(k)}2 \tag{A15}$$

where i takes on all $N_I = (n^4 + 3n^2 - 2n)/4$ admissible pairs of intersection points, while j and k correspond to the indexed receiver pairs. We also define the $N_I \times 1$ vector

$$\mathbf{T} = \left[2\tau_{jk}^{(1)}\left(\tau_j^{(1)} - \tau_k^{(1)}\right), \ldots, 2\tau_{jk}^{(N_I)}\left(\tau_j^{(N_I)} - \tau_k^{(N_I)}\right)\right]^T \tag{A16}$$

and the 3×1 vector

$$\mathbf{X} = [C/E, B/E, A/E]^T \tag{A17}$$

where

$$E = \boldsymbol{V}_{\mathbf{eff}}^2\left(AC - B^2/4\right) \tag{A18}$$

Now, the system of equations described by euation (A11) can be written in matrix form as

$$\mathscr{D}\mathbf{X} = \mathbf{T} \tag{A-19}$$

which has the least squares solution

$$\widehat{\mathbf{X}} = \left[\mathscr{D}^T\mathscr{D}\right]^{-1}\mathscr{D}^T\mathbf{T} \tag{A20}$$

Note that knowing $\widehat{\mathbf{X}} \approx [C/E, B/E, A/E]^T$ is equivalent as knowing $\left[\mathscr{E}/\boldsymbol{V}_{\mathbf{eff}}^2\right]$, since

$$\frac{\mathscr{E}}{\boldsymbol{V}_{\mathbf{eff}}^2} = \frac{1}{\boldsymbol{V}_{\mathbf{eff}}^2(AC - B^2/4)}\begin{bmatrix} C & -B/2 \\ -B/2 & A \end{bmatrix} = \begin{bmatrix} C/E & -B/2E \\ -B/2E & A/E \end{bmatrix} \tag{A21}$$

Based on equation (A9), the following relationship can be established

$$\boldsymbol{V}^{\boldsymbol{D}^T}\left[\mathscr{E}/\boldsymbol{V}_{\mathbf{eff}}^2\right]\left(\Delta\boldsymbol{\rho}^{(j)} - \Delta\boldsymbol{\rho}^{(k)}\right) = \tau_j - \tau_k \tag{A22}$$

As discussed before, we now can solve this system of equations using the solved $\left[\mathscr{E}/\boldsymbol{V}_{\mathbf{eff}}^2\right]$. Similarly, we first define the $N_I \times 2$ matrix

$$\mathscr{I} = \begin{bmatrix} I_x^{(1)} & I_y^{(1)} \\ \vdots & \vdots \\ I_x^{(N_I)} & I_y^{(N_I)} \end{bmatrix} \tag{A23}$$

where

$$I_x^{(i)} = \frac{C}{E}\left(\Delta\rho_x^{(j)} - \Delta\rho_x^{(k)}\right) - \frac{B}{2E}\left(\Delta\rho_y^{(j)} - \Delta\rho_y^{(k)}\right) \tag{A24}$$

$$I_y^{(i)} = -\frac{B}{2E}\left(\Delta\rho_x^{(j)} - \Delta\rho_x^{(k)}\right) + \frac{A}{E}\left(\Delta\rho_y^{(j)} - \Delta\rho_y^{(k)}\right) \tag{A25}$$

and the $N_I \times 1$ vector $\boldsymbol{\chi}$ with elements

$$\chi^{(i)} = \tau_j^{(i)} - \tau_k^{(i)} \tag{A26}$$

together with the 2×1 vector $\boldsymbol{V^D} = \left[\boldsymbol{V_x^D}, \boldsymbol{V_y^D}\right]^T$ to be solved for.

Equation (A22) can now be written in matrix form as

$$\mathcal{J}\boldsymbol{V^D} = \boldsymbol{\chi} \tag{A27}$$

which has the least squares solution

$$\widehat{\boldsymbol{V^D}} = \left[\mathcal{J}^T\mathcal{J}\right]^{-1}\mathcal{J}^T\boldsymbol{\chi} \tag{A28}$$

Equations (A20) and (A28) give the scaled anisotropy by $\boldsymbol{V}_{\mathbf{eff}}^2$ and the diffraction pattern velocity derived from a set of receiver temporal correlation functions.

Acknowledgments

This project is supported by an AFOSR grant (FA9550-14-1-0265). The GNSS receiver array data are collected with the help of Steve Taylor and Harrison Bourne of the Satellite Navigation and Sensing (SeNSe) Lab at the University of Colorado at Boulder. The PFISR data are acquired from the Madrigal database (http://isr.sri.com/madrigal). The Poker Flat Incoherent Scatter Radar is operated by SRI International on behalf of the U.S. National Science Foundation under NSF Cooperative Agreement AGS-1133009. The *Kp*, *AE*, and *Dst* indices are obtained from the World Data Center for Geomagnetism operated by the Kyoto University (http://wdc.kugi.kyoto-u.ac.jp). The interplanetary and geophysical parameters are obtained from NASA/GSFC's Space Physics Data Facility's OMNIWeb service (http://omniweb.gsfc.nasa.gov/index.html). The magnetometer data were obtained from the Geophysical Institute Magnetometer Array online service (http://magnet.gi.alaska.edu). The authors also wish to thank Dr. Don Hampton at the University of Alaska Fairbanks for sharing the ASI data and staff at the Poker Flat for hosting the GNSS array.

References

Anderson, D. N., & Mendillo, M. (1983). Ionospheric conditions affecting the evolution of equatorial plasma depletions. *Geophysical Research Letters*, *10*(7), 541–544. https://doi.org/10.1029/GL010i007p00541

Armstrong, J. W., & Coles, W. A. (1972). Analysis of three-station interplanetary scintillation. *Journal of Geophysical Research*, *77*(25), 4602–4610. https://doi.org/10.1029/JA077i025p04602

Basu, S., & Basu, S. (1981). Equatorial scintillations—A review. *Journal of Atmospheric and Terrestrial Physics*, *43*(5-6), 473–489. https://doi.org/10.1016/0021-9169(81)90110-0

Basu, S., Basu, S., Kuoeki, E., Zengingonul, H. P., Biondi, M. A., & Meriwether, J. W. (1991). Zonal irregularity drifts and neutral winds measured near the magnetic equator in Peru. *Journal of Atmospheric and Terrestrial Physics*, *53*(8), 743–755. https://doi.org/10.1016/0021-9169(91)90125-Q

Basu, S., Kudeki, E., Basu, S., Valladares, C. E., Weber, E. J., Zengingonul, H. P., et al. (1996). Scintillations, plasma drifts, and neutral winds in the equatorial ionosphere after sunset. *Journal of Geophysical Research*, *101*(A12), 26,795–26,809. https://doi.org/10.1029/96JA00760

Briggs, B. H. (1968). On the analysis of moving patterns in geophysics—I. Correlation analysis. *Journal of Atmospheric and Terrestrial Physics*, *30*(10), 1777–1788. https://doi.org/10.1016/0021-9169(68)90097-4

Briggs, B. H., Phillips, G. J., & Shinn, D. H. (1950). The analysis of observations on spaced receivers of the fading of radio signals. *Proceedings of the Physical Society. Section B*, *63*(2), 106–121. https://doi.org/10.1088/0370-1301/63/2/305

Carrano, C. S., Groves, K. M., Rino, C. L., & Doherty, P. H. (2016). A technique for inferring zonal irregularity drift from single-station GNSS measurements of intensity (S4) and phase (σφ) scintillations. *Radio Science*, *51*, 1263–1277. https://doi.org/10.1002/2015RS005864

Costa, E., Fougere, P. F., & Basu, S. (1988). Cross-correlation analysis and interpretation of spaced-receiver measurements. *Radio Science*, *23*(2), 141–162. https://doi.org/10.1029/RS023i002p00141

Fedor, L. S. (1967). A statistical approach to the determination of three-dimensional ionospheric drifts. *Journal of Geophysical Research*, *72*(21), 5401–5415. https://doi.org/10.1029/JZ072i021p05401

Ji, S., Chen, W., Ding, X., & Zhao, C. (2011). Equatorial ionospheric zonal drift by monitoring local GPS reference networks. *Journal of Geophysical Research*, *116*, A08310. https://doi.org/10.1029/2010JA015993

Khudukon, B. Z., Tereshchenko, E. D., Galinov, A. V., Popov, A. A., & Nygren, T. (1994). Determination of drift velocity and anisotropy of irregularities in the auroral ionosphere using radio source scintillation. *Journal of Atmospheric and Terrestrial Physics*, *56*(1), 93–102. https://doi.org/10.1016/0021-9169(94)90179-1

Kil, H., Kintner, P. M., de Paula, E. R., & Kantor, I. J. (2002). Latitudinal variations of scintillation activity and zonal plasma drifts in South America. *Radio Science*, *37*(1), 1006. https://doi.org/10.1029/2001RS002468

Kil, H., Kintner, P. M., Paula, E. R., & Kantor, I. J. (2000). Global positioning system measurements of the ionospheric zonal apparent velocity at Cachoeira Paulista in Brazil. *Journal of Geophysical Research*, *105*(A3), 5317–5327. https://doi.org/10.1029/1999JA000244

Kintner, P. M., Ledvina, B. M., De Paula, E. R., & Kantor, I. J. (2004). Size, shape, orientation, speed, and duration of GPS equatorial anomaly scintillations. *Radio Science*, *39*, RS2012. https://doi.org/10.1029/2003RS002878

Mendillo, M., & Baumgardner, J. (1982). Airglow characteristics of equatorial plasma depletions. *Journal of Geophysical Research*, *87*(A9), 7641–7652. https://doi.org/10.1029/JA087iA09p07641

Mitra, S. N. (1949). A radio method of measuring winds in the ionosphere. *Proceedings of the IEE-Part III: Radio and Communication Engineering*, *96*(43), 441–446.

Rino, C. L., & Fremouw, E. J. (1977). The angle dependence of singly scattered wavefields. *Journal of Atmospheric and Terrestrial Physics*, *39*(8), 859–868. https://doi.org/10.1016/0021-9169(77)90166-0

Rino, C. L., & Livingston, R. C. (1982). On the analysis and interpretation of spaced-receiver measurements of transionospheric radio waves. *Radio Science*, *17*(4), 845–854. https://doi.org/10.1029/RS017i004p00845

Secan, J. A., Bussey, R. M., Fremouw, E. J., & Basu, S. (1995). An improved model of equatorial scintillation. *Radio Science*, *30*(3), 607–617. https://doi.org/10.1029/94RS03172

Singleton, D. G. (1970). Saturation and focusing effects in radio-star and satellite scintillations. *Journal of Atmospheric and Terrestrial Physics*, *32*(2), 187–208. https://doi.org/10.1016/0021-9169(70)90191-1

Spatz, D. E., Franke, S. J., & Yeh, K. C. (1988). Analysis and interpretation of spaced receiver scintillation data recorded at an equatorial station. *Radio Science*, *23*(3), 347–361. https://doi.org/10.1029/RS023i003p00347

Su, Y., Datta-Barua, S., Bust, G. S., & Deshpande, K. B. (2017). Distributed sensing of ionospheric irregularities with a GNSS receiver array. *Radio Science*, *52*, 988–1003. https://doi.org/10.1002/2017RS006331

Thébault, E., Finlay, C. C., Beggan, C. D., Alken, P., Aubert, J., Barrois, O., et al. (2015). International geomagnetic reference field: The 12th generation. *Earth, Planets and Space*, *67*(1), 1–19.

Vacchione, J. D., Franke, S. J., & Yeh, K. C. (1987). A new analysis technique for estimating zonal irregularity drifts and variability in the equatorial F region using spaced receiver scintillation data. *Radio Science*, *22*(5), 745–756. https://doi.org/10.1029/RS022i005p00745

Wang, J., Morton, Y. J., & Hampton, D. (2018). New results on ionospheric irregularity drift velocity estimation using multi-GNSS spaced-receiver Array during high-latitude phase scintillation. *Radio Science*, *53*, 228–240. https://doi.org/10.1002/2017RS006470

Wang, J., & Morton, Y. T. (2015). High-latitude ionospheric irregularity drift velocity estimation using spaced GPS receiver carrier phase time–frequency analysis. *IEEE Transactions on Geoscience and Remote Sensing*, *53*(11), 6099–6113. https://doi.org/10.1109/TGRS.2015.2432014

Wang, J., & Morton, Y. T. (2017). A comparative study of ionospheric irregularity drift velocity derived from a GNSS receiver Array and PFISR measurements during high latitude ionospheric scintillation. *Journal of Geophysical Research: Space Physics*, *122*, 6858–6881. https://doi.org/10.1002/3028JA024015